Subpixel Melt Index In Antarctic Peninsula Using Spatially Constrained Linear Unmixing From Time Series Satellite Passive Microwave Images

Dan Tian[1] and Lei Wang[1*]

[1] Department of Geography & Anthropology, Louisiana State University, Baton Rouge, LA 70810.

*Corresponding author: Lei Wang (leiwang@lsu.edu) https://orcid.org/0000-0003-1298-4839

Key Points:

- The overestimation of the Boolean surface melt maps in the Antarctic Peninsula could be as large as 56%.
- The least squares mixture analysis offers to offset the bias in the Boolean surface melt maps created from satellite radiometers.
- Elevation plays an important role in the partial melting. phenomenon on Antarctic ice sheets.

Abstract

The inevitable coarse pixels (~25 km) of satellite passive microwave images introduced large uncertainty to the surface melt area estimation on Antarctic ice margins. Our test showed that the melt index of the Austral year 2012-13 in the Antarctic Peninsula calculated from the high resolution product was 33% lower than the original Special Sensor Microwave/Imager (SSM/I) images. Therefore, by allowing for fractional melt estimation, a subpixel mapping method was adopted in this research to improve the accuracy and reliability of surface melt measurement from passive microwave images. This innovative method uses the least squares mixture analysis (LSMA) on the time series of daily passive microwave images by taking advantage of their high temporal resolution. The endmembers for the unmixing calculation were collected under the constraint of voronoi polygons. The fractional melt index of each pixel was calculated by multiplying its area with melt fraction. By using the high resolution passive microwave earth system data record (PMESDR) dataset as the reference, we found that compared with the original SSM/I images, the overestimation of surface melt was corrected by the unmixing analysis. A log-linear regression between melt fraction and elevation showed that the melt fraction is inversely correlated to the elevation, and the topography is the dominant factor for melt fraction distribution in high elevations. We recommend such a treatment of linear unmixing analysis on the passive microwave images to be used for future surface melt mapping in Antarctica and Greenland.

Plain Language Summary

Surface melt could be one of the major causes of the recent and historical disintegration of Antarctic ice shelves. Tracking and monitoring surface melt from satellites are crucial to better understanding of how the regional and global climate is changing and the relationship between climate change and glacier dynamics. However, none of the current satellites provides sufficiently detailed data for scientists to measure surface melt with high confidence and accuracy. We found that the current estimation of surface melt in the Antarctic Peninsula could be 56% larger than its actual value because of the signal mixing problem. Therefore, we propose a subpixel estimating method that is able to offset the overestimation problem in the previous research. The new melt map was proved more accurate and reliable for interannual trend analysis.

1. Introduction

Mapping surface melt on Antarctic Ice Shelves is of great significance for studying glacier dynamics and regional and global climate changes. Melting snow has a low visible and near-infrared albedo, absorbing up to four times as much solar radiation as dry snow (Steffen, 1995). In addition, percolating melt water accelerates iceberg calving and causes ice mass loss and ice front retreat (Holland, 2010). Antarctica Ice Shelves are sensitive to the warming temperature. As shown in Zwally and Fiegles (1994), surface melt intensity is related to the locally accumulative number of days above the melting temperature. Consistent and intense surface melt contributed to enlarged ice crevasses (Scambos et al., 2000), accelerated glacier flow (Zwally, 2002), and disintegration of ice tongues (van den Broeke, 2005). Monitoring surface melt phenomena is a key to understanding regional and global climate changes (Doake & Vaughan, 1991; Gilbert & Domack, 2003; MacAYEAL et al., 2003; Vaughan & Doake, 1996).

Antarctica has the highest winds, lowest temperatures, and highest average elevation on Earth. Severe weather, poor accessibility, long and dark polar nights in winter, and logistical difficulties give rise to serious challenges to traditional field observations. Satellite passive microwave data capture surface emission from water, vegetation, soil, and snow and ice under all weather conditions, and have become the only data source capable of continuously monitoring surface melt in Antarctica (Liu et al., 2006) for long terms. The Defense Meteorological Satellite Program (DMSP) operated by National Oceanic and Atmospheric Administration (NOAA) has launched a series of satellites since 1978 with the payload of multiple generation passive microwave sensors including scanning multichannel microwave radiometer (SMMR), Special Sensor Microwave/Imager (SSM/I), and Special Sensor Microwave Imager Sounder (SSMIS). Glacier and ice sheet surface melting was mapped from this dataset for Greenland (Abdalati & Steffen, 1995, 1997, 2001; Liang et al., 2019; Mote et al., 1993; Mote & Anderson, 1995) and Antarctica (Fahnestock et al., 2002; Liang et al., 2019; Liu et al., 2006; Ridley, 1993; Torinesi et al., 2003; Zwally & Fiegles, 1994).

Large Instantaneous field of view is required for passive microwave sensors to achieve sufficient signal-to-noise ratio from satellite orbits that are usually placed at 700~800 km above the ground elevation. The nominal ground spacing of the SSM/I pixels obtained at the 19 GHz channel, for example, is 25 km. In other words, any ground objects or processes that are smaller than 25 km will not be accurately measured. Therefore, uncertainty due to the large pixel size exists in the melt maps derived at the 25 km scale and could be large enough to distort our knowledge of climate changes derived from the melt maps. Consistent decreasing trends of surface melt over the Antarctic continent were reported by different research groups using the satellite passive microwave data (Liang et al., 2019; Liu et al., 2006; Tedesco, 2009; Wang & Liu, 2017). These reported trends, however, were contradictory to the warming climate records in Antarctica (Steig et al., 2009) and increasing sea levels caused by ice sheet melt (Golledge et al., 2019). The uncertainty of surface melt records from the passive microwave data could contribute to such inconsistency between the surface melt trend in Antarctica and other climatological reports. The work by De Freitas et al. (2018) suggested that the Boolean classification of melt and non-melt status of the large SSM/I pixels would overestimate melt extents. They proposed an unmixing method using four channels (19H, 19V, 37H, and 37V) of

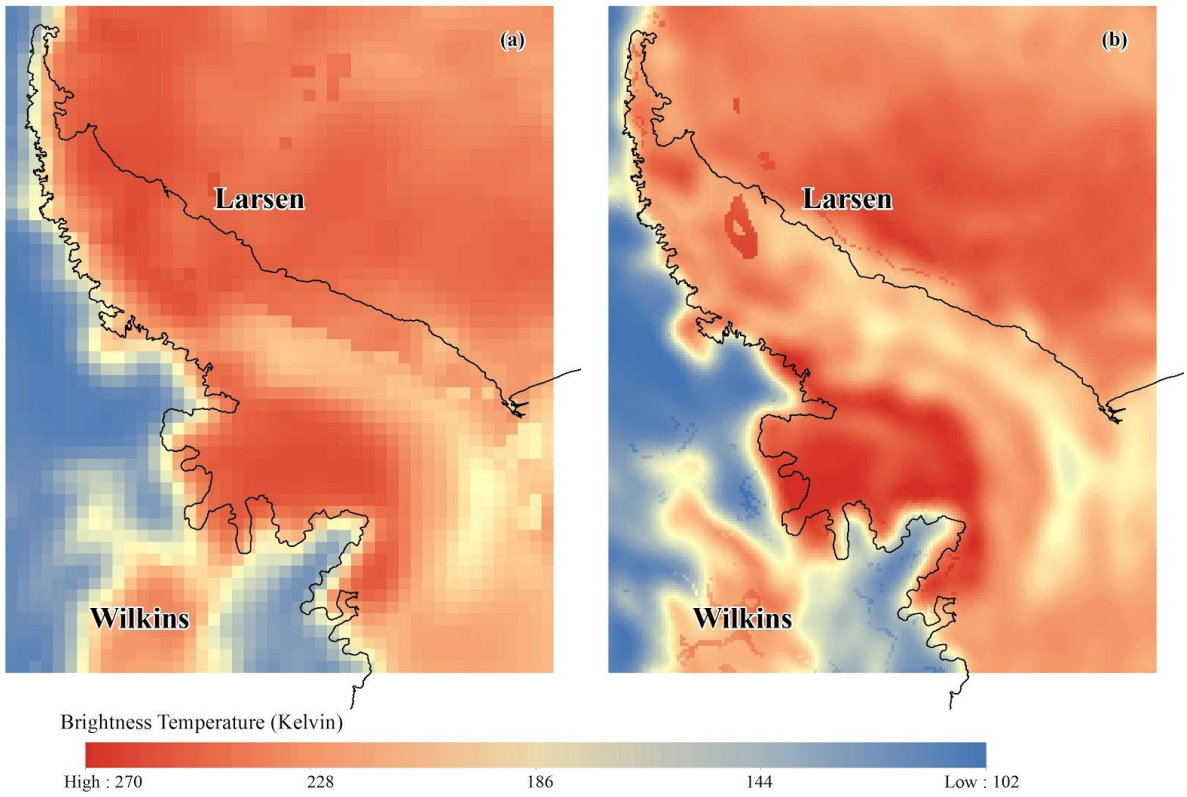

Figure 1: Study area of the Antarctic Peninsula. (a) The SSM/I image and (b) the PMESDR image of December 31, 2012

SSM/I to unmix three endmembers: wet snow, dry snow, and rock outcrops. Their method, however, is limited by the number of channels and cannot unmix more than three endmembers. And the high similarity among the four channels in their responses to melting and non-melting status compromises the unmixing model premise. The brightness temperature of dry snow can range from 175 K to 235 K because of the large variation of the emissivity, which is strongly dependent on the grain-size (Zwally & Fiegles, 1994). Therefore, it is difficult to determine pure dry endmembers only based on the absolute brightness temperature. In this research, we propose a new unmixing algorithm that (1) treats the time series brightness temperature data as hyperspectral images and (2) identifies endmembers by searching distances. The objective of this paper is twofold: (1) to quantify the overestimation bias of the existing SSM/I surface melt maps and (2) to verify that our new unmixing method can reduce the uncertainty and correct the bias of melt map production from passive microwave remote sensing data.

2. Data and study area

Figure 1 shows the boundary and coastline of the study area overlaid with the SSM/I image (a) and the PMESDR image (b) of December 31, 2012. The study area is measured as 1,150 km by

1,400 km, with 584,375 km^2 of land surface area. The passive microwave images were obtained by the Special Sensor Microwave/Imager (SSM/I) onboard the Defense Meteorological Satellite Program (DMSP) satellites, which measures microwave brightness temperature of the atmosphere, ocean, and terrain (NOAA, 2019). It offers daily data since 1987 in vertical polarization 22.235 GHz and both horizontal and vertical polarization 19.35, 37.0, and 85.5 GHz (Armstrong et al., 1994). Among the 7 channels, Liu et al. (2006) made a comparison of the brightness temperature of different frequencies and polarizations and found that the low frequency channels were more sensitive to melt initiation than the channels at higher frequencies. This is mainly because both absorption and emission of microwave radiation are stronger at higher frequency. About polarization, according to Abdalati and Steffen (1997) and Liu et al. (2006), at the same frequency, the conversion from dry snow to wet snow leads to a greater increase in the brightness temperature of horizontal polarization than that of vertical polarization. Based on these findings, the brightness temperature data at the satellite ascending nodes from July 1, 2012 to June 30, 2013 at the 19 GHz frequency with the horizontal polarization were chosen for this study.

For validation of the subpixel fraction derived from the unmixing algorithm, we used the enhanced resolution passive microwave earth system data record (PMESDR) produced from the MEaSUREs program funded by NASA, which used the proven interpolation method (David G. Long & Brodzik, 2016; D. G. Long & Daum, 1998) to reprocess and fuse the complete data records of SMMR, SSM/I-SSMIS and AMSR-E in a single grid passive microwave ESDR with improved resolution. The interpolation algorithm takes advantage of overlapping and oversampling satellite IFOVs to reconstruct the high resolution image (Brodzik & Long, 2015). The dataset we used was the calibrated enhanced resolution passive microwave daily grid 2.0 brightness temperature ESDR, version 1 (CETB) ESDR using the latest improved level 2 SSM/I-SSMIS and AMSR-E data recording (Brodzik et al., 2018). For channel 19H, the best resolution achieved by the interpolation is 6.25 km, which is set by the 25-km base resolution and power-of-2 dividers. Therefore, each original SSM/I pixel is nested by 16 PMESDR pixels. We use the melt fraction derived from each set of 16 PMESDR pixels to verify the melt fraction calculated from the least squares mixture analysis described below.

3. Methods

3.1. Melt detection

On ice sheets and ice shelves, passive microwave sensors detect naturally emitted microwave energy from both dry and melting snows within their field of view. Measured passive microwave data is in the form of brightness temperature calibrated based on the recorded microwave energy. The relationship between the calculus brightness temperature (T_b) and the near-surface physical temperature (T_s) can be expressed by first-order Rayleigh-Jeans approximation (Zwally & Gloersen, 1977) in the microwave spectra:

$$T_b = \varepsilon \cdot T_s \tag{1}$$

where ε is the emissivity of snow near the surface. The emissivity of wet snow in the microwave region is about 0.9, while that of dry snow varies from 0.65 to 0.85, which is depending on the

particle size, because the scattering by ice grains of the radiation emitting from deeper layers in snow packs will reduce the emissivity. Therefore, assuming the temperature at the melting point of ice (273.6 K), the theoretical brightness temperature of wet snows is 246 K, which is about 15 to 70 degrees above the brightness temperature of dry snows (Zwally & Fiegles, 1994). When dry snow packs start to melt, the brightness temperature will rise drastically even if the physical temperature does not change. Similarly, brightness temperature will drop back to the premelting status when the snow packs refreeze. Microwave sensors with a frequency higher than 10 GHz can detect the increase and decrease of brightness temperature when snow begins to melt and refreezes, respectively (Liu et al., 2006). Such brightness temperature changes, rather than physical temperature fluctuations, can be used to track the melt and refreeze events during an austral summer from satellite observations.

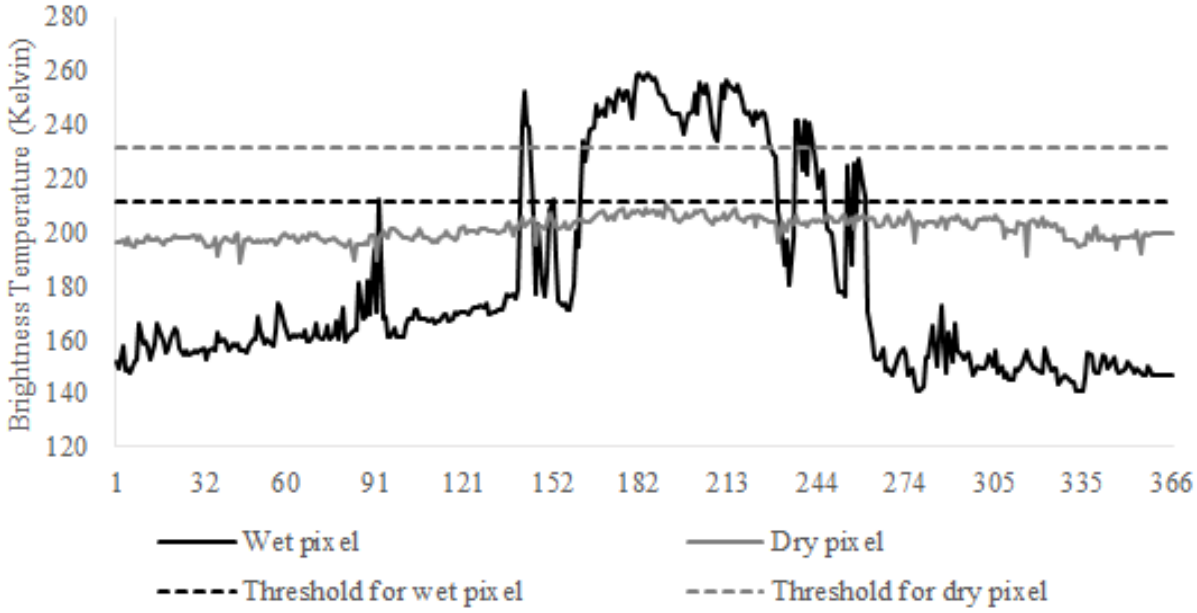

Figure 2: The annual variations of brightness temperature for typical wet and dry pixels under the 19 GHz horizontal channel of the SSM/I data

For better generalizability, the algorithm for melt detection is chosen as the one proposed by Zwally and Fiegles (1994) rather than the sophisticated edge detection methods such as Liu et al. (2005). In Zwally and Fiegles (1994), a local mean T_b plus 30 degrees (noted as ZF+30) was used as the melt detection threshold for each pixel. This algorithm takes the spatial variation of dry snow emissivity into consideration and allows the threshold values to be adaptive to the local conditions. Figure 2 compared the time series of a wet pixel (pixel that experienced melt in the year) and a dry pixel (pixel that did not melt in the year), along with the Zwally and Fiegle threshold (ZF+30) lines for melt detection in both time series. Thus, the melt detection algorithm assigned 73 melting days to the wet pixel and 0 melting day to the dry pixel. The melt index (*MI*) of the wet pixel at the 25 km cell size, as a variable used for multi-year trend analysis of surface melt, is then computed as: 73 day × 625 km^2= 45,625 day·km^2.

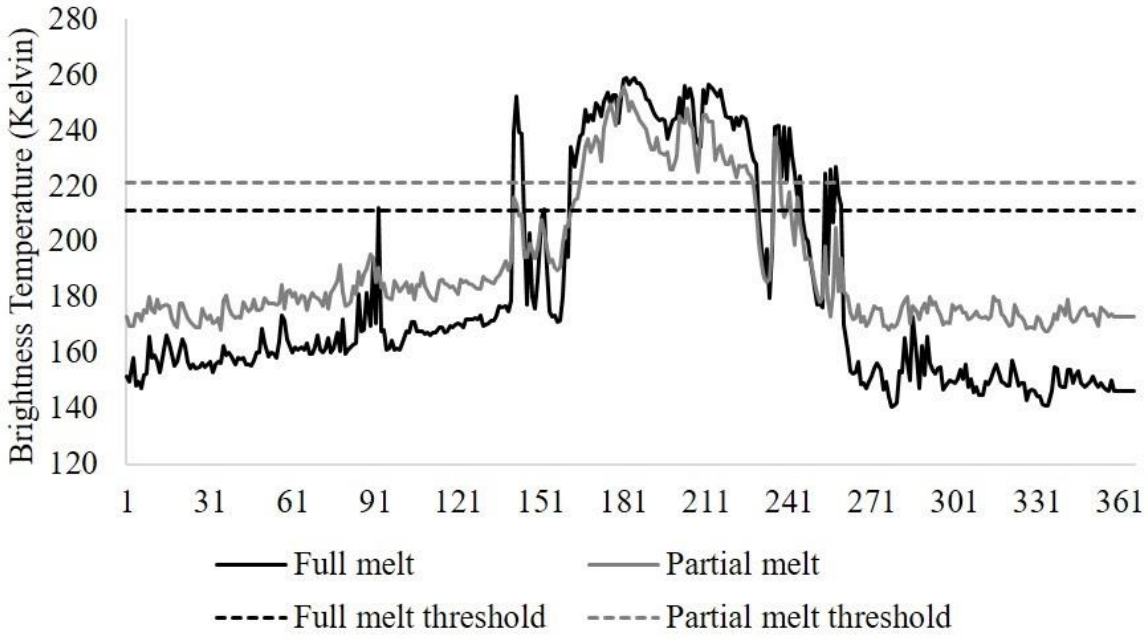

Figure 3: The annual variations of brightness temperature for typical full melt and partial melt pixels under the 19 GHz horizontal channel of the SSM/I data.

3.2. Least squares mixture analysis of partial melt data

Figure 3 illustrates a full melt pixel and a partial melt pixel and their melt detection thresholds. The melt index for the full melt pixel is 55,625 day·km^2, and the partial melt pixel is 40,000 day·km^2. The partial melt pixel had a similar threshold value as the full melt pixel according to Zwally and Fiegles (1994). However, because the pixel is a mix of melt and none-melt subregions within the pixel, the brightness temperature at the melt status did not rise higher than the threshold. The dilemma arises for melt days calculation: do we need to decrease the threshold to assign higher *MI* for the partial melt pixel or decrease the *MI*? From the time series view, it seems the melt duration was underestimated in the illustrated partial melt pixel. To correct the problem of underestimation, a lower threshold should be proposed, which requires the knowledge of each partial melt pixel. Even if the new threshold was assigned, in the spatial point of view, the Boolean assignment of melt overestimates the melt index because only a fraction of the 25 km by 25 km pixel actually experienced melting.

In figure 3, the full melt pixel and the partial melt pixel have similar shapes of their time series plots, indicating the synchronization of the two pixels in melting occurrence due to their closeness in distance. The difference of the wet snow brightness temperature in these two plots is presumed to be related to the signal mixture phenomenon. Explicitly, the wet snow brightness temperature of a partial melting pixel in a time series $T_{p,t}$ is a linear combination of the brightness temperature of melting part $T_{m,t}$ and non-melting component $T_{n,t}$ for t = 1,2,3…,365 (or 366 in a leap year), as expressed by equation 2:

$$T_{p,t} = \alpha_m T_{m,t} + \alpha_n T_{n,t} + \varepsilon \quad (2)$$

where α_m is the fraction of the melting area; α_n is the fraction of the non-melting area; ε is the error term. The least-square solution, which minimizes the error term, under the constraints of unity and positiveness (Chein-I Chang et al., 2004), was used to solve the equation. Once the melt fraction is calculated, the melt area can be updated by multiplying the total area of an SSM/I pixel and the fraction number. For example, if a pixel is 50% melt, the total melt area from that pixel is 25 km × 25 km × 50% = 312.5 km^2 instead of 625 km^2.

3.3. Endmember selection

In equation 2, endmembers of melt and non-melt time series should be provided to obtain the solution of melt and non-melt fraction for each partial melt pixel. Endmembers are defined as pure pixels, which represent the information of a homogenous phenomenon such as melting or non-melting. $T_{n,t}$ is the time series of a non-melt pixel in a year. $T_{m,t}$ is the time series of a full melt pixel. It is relatively easy to find the non-melt pixels by using the ZF+30 criterion. However, as shown in figure 3, both the full melt and partial melt pixels were over the line of the ZF+30 criterion. Therefore, the ZF+30 criterion cannot separate full melt and partial melt pixels. However, as can be observed from figure 3, the melt edges of the full melt pixel is greater than those of the partial melt pixel because the mixture of melt and non-melt signal tends to reduce the magnitude of these edges.

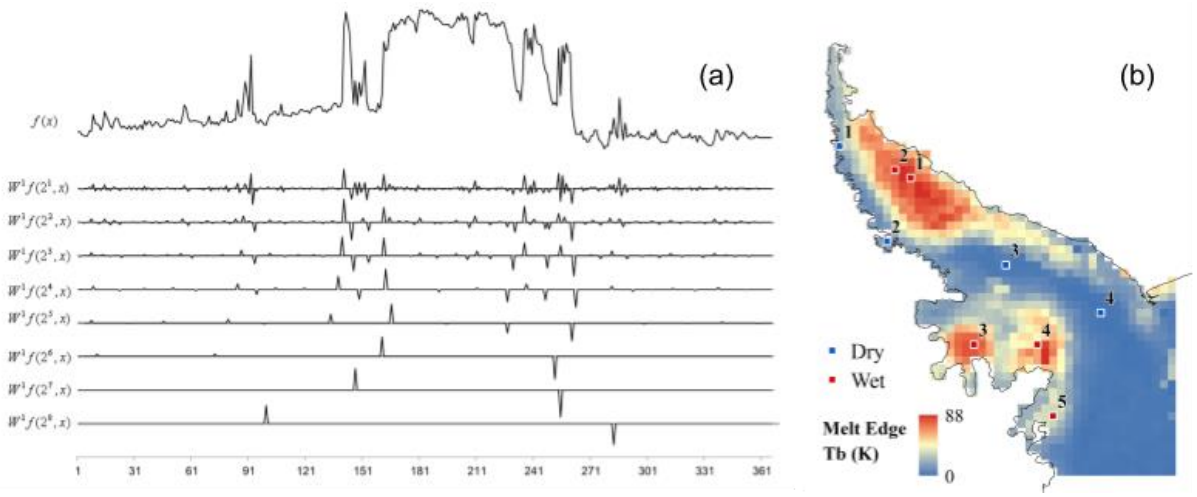

Figure 4: (a) The original daily time series of endmember wet #3 and its wavelet transformation local maxima (Liu et al., 2005) at all scales. Particularly, $W^1f(2^4,x)$ at the fourth scale was used to classify the edges to large (GL) and small (GS) groups. (b) Locations and labels of the five full melt endmembers and four non-melt endmembers and their mean GL edge strength map. The full melt endmembers were selected from the locations with high GL strengths and the non-melt endmembers were selected from the low GL strength areas.

It is not difficult to run a wavelet decomposition and use a bimodal classification method to differentiate melt edges from non-melt edges at the fourth wavelet scale (Liu et al., 2005). Figure 4 (a) shows the time series of wet endmember #3 (figure 4b) and its wavelet transformation local maxima used to track melt occurrences (Liu et al., 2005). The wavelet transformation filtered the noise component and preserved stronger edges at higher scales as

indicators of melt events. The bimodal classification sorts the edges by their magnitude and groups them to two classes - large (GL) and small (GS). The goal is to minimize the in-group variance and maximize the between-group variance (Liu et al., 2005). For a wet pixel, GL contains the edges caused by melt signals, while GS contains the edges caused by temperature fluctuations. For non-melt pixels, both groups are non-melt edges, which are low in magnitude. Therefore, the mean magnitude of the GL of a non-melt pixel is much lower than that of melt pixels. The mean magnitude of the GL was used as an indicator of pixel purity: the larger the mean GL edge magnitude, the more likely the pixel to be a pure melt pixel. Figure 4 (b) shows the GL edge magnitude map in the study area and the locations of wet and dry endmembers. Indeed, all the red-colored pixels could be considered as areas of full melt. We picked the most representative ones as endmembers. The blue-colored area contains non-melt (dry) endmembers. Yellow colors represent mixed pixels. We selected these endmembers to run the least squares mixture analysis for melt fraction calculation within each 25-km SSM/I pixel. Melt edges are clearly much stronger than non-melt edges, not only in the magnitude but also in the temporal continuity. The endmembers are defined locally because the shape of the time series brightness temperature changes from region to region. Each melt event is bounded by a certain terrain boundary such as ridges of high mountains on ice sheets. On the other hand, the melt events on ice shelves could extend far because of the flat topography. For each mixed pixel, the wet and dry endmembers were picked from a tessellation of voronoi polygons defined by the locations of endmembers (figure 5). Each voronoi polygon defines the nearest neighbor area to the endmember candidates. Mixed pixels located within the polygon defined by an endmember will be unmixed from it. The tessellation map of figure 5(a) is for wet endmember selection. The tessellation map of figure 5(b) is for dry endmember selection. The nearest neighbor zones assign one wet endmember based on figure 5(a) and one dry endmember based on figure 5(b) to the partial melting pixels. With the wet and dry endmembers, the fraction of the melt and non-melt area in each partial melting pixel were computed using equation 2.

3.4. Accuracy Assessment

To verify the unmixing model, we employed the high resolution product of passive microwave earth system data record (PMESDR) program. The product was created by fusing multiple passive microwave observations from overlapping orbits of the same sensor and/or different sensors to reconstruct the super-resolution brightness temperature data. In terms of the spatial resolution, this product is comparable to another high resolution product from the QUIKSCAT satellite SeaWinds Ku band radar image using a similar high-resolution reconstruction algorithm. In fact, the super-resolution QUIKSCAT product was used for accuracy assessment in many snow melt mapping projects (Bhattacharya et al., 2009; De Freitas et al., 2018). However, the problem of QUIKSCAT data is its short life. It collected global images from 1999 to 2009 for about ten years, which already exceeded its designed life. The PMESDR program created super-resolution passive microwave images spanning much longer time than QUIKSCAT, and because it is a product of radiometers rather than scatterometers, it is superior to QUIKSCAT images for verifying the unmixing algorithm on passive microwave images.

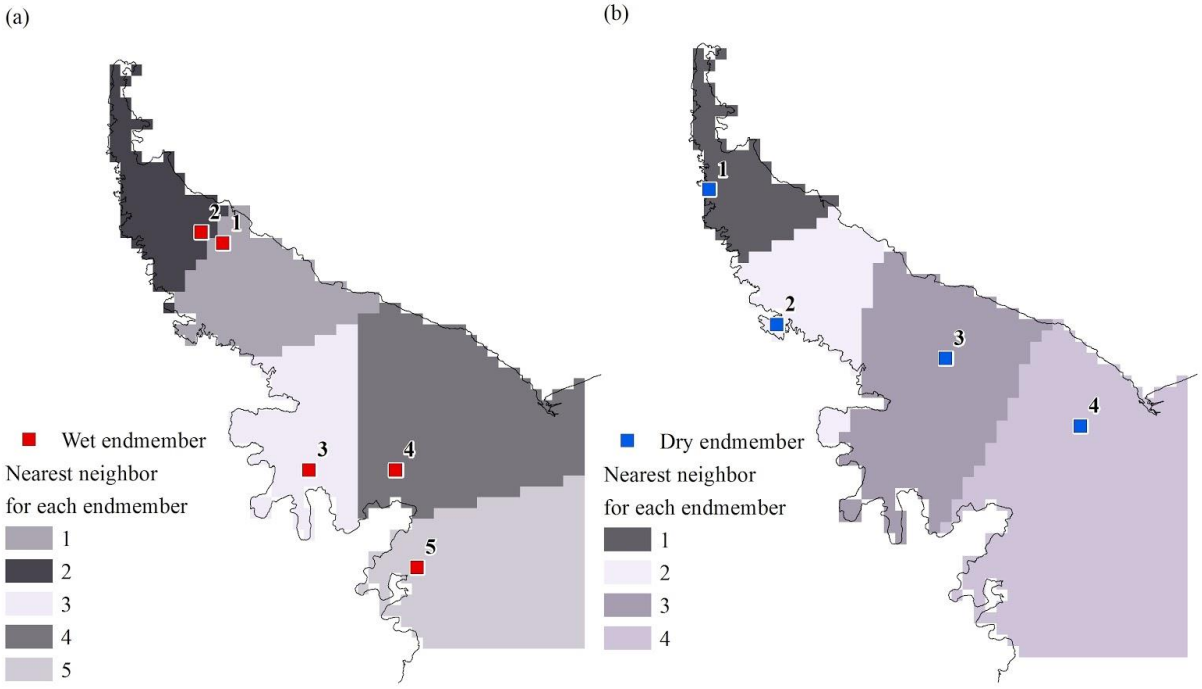

Figure 5: Spatially constrained endmember selection defined by voronoi polygons

The comparison between the model output and the high resolution data used the melt index (*MI*) variable derived from the time series of passive microwave data. Melt index (in day·km^2) is the sum of the daily melt extents for a certain area (e.g. the entire Antarctica or the Antarctic Peninsula) for the entire season (Liu et al., 2006). Melt index is a convenient variable to study the interannual trends of surface melt in Antarctica and Greenland and an indicator for climate change (Bhattacharya et al., 2009; Liu et al., 2006; Oza, 2015; Tedesco, 2009). The formula of the melt index is:

$$MI = \sum_{i=1}^{n} md_i \cdot A \tag{3}$$

where A is the area size of one pixel (assuming it is a constant for all pixels), N is the total number of pixels, and md_i is the number of melt days (melting duration) within a year for the pixel i. Each 25 km × 25 km SSM/I pixel contains 16 high resolution PMESDR pixels (6.25 km × 6.25 km). The total *MI* of the 16 PMESDR pixels was compared to the unmixed SSM/I pixel *MI*. The sum of *MI* for the entire study area as well as the root mean square error (RMSE) from pixel-wise comparison of all the land pixels were reported in table 1.

4. Results and discussions

4.1. Linear mixture analysis and accuracy assessment

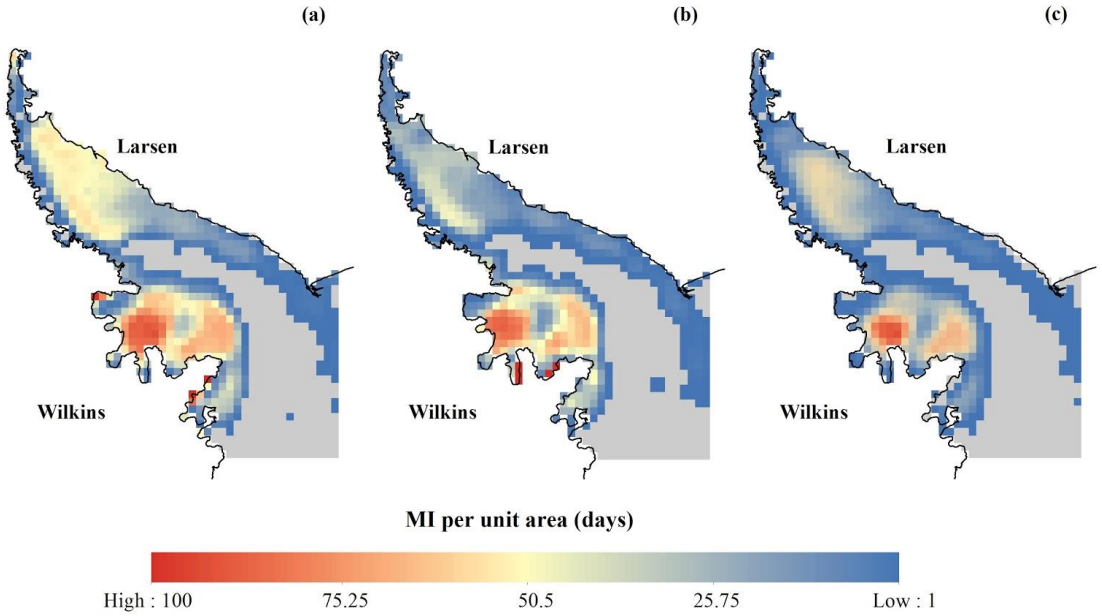

Figure 6: Comparing *MI* of (a) original SSM/I, (b) PMESDR, and (c) LSMA result.

Table 1 summarizes the total melt index of the Antarctic Peninsula and pixel-wise statistical values calculated from the three datasets: (1) original SSM/I (2) unmixed SSM/I from LSMA, and (3) high-resolution PMESDR images. The total melt index of the entire study area in the Austral summer of 2012-13 differed from each other. The melt index calculated from the original SSM/I data is about 50% larger than that from PMESDR, showing that there was a significant bias of overestimation of the reported surface melt using the original SSM/I data. The *MI* of the least squares mixture analysis (LSMA) was 43% smaller than the original SSM/I data and slightly (14%) smaller than the PMESDR result.

Table 1: Comparison of *MI* from different datasets and their RMSE referenced to PMESDR data.

Melt index (10^6 day·km^2)	**SSM/I**	**LSMA**	**PMESDR**
Study area total	11.365	6.478	7.565
RMSE	0.0104	0.0083	N/A

The lower RMSE of the LSMA result indicates that the subpixel melt index improved the confidence and accuracy over the Boolean calculation of melt index from SSM/I images. The 14% lower *MI* of the unmixed SSM/I data is also justifiable, because later in the discussion 4.4 we will show the LSMA result from the PMESDR images, which was further lower than the

Boolean calculation from PMESDR data. In other words, overestimation also exists in the high resolution PMESDR images. Therefore, the 14% lower MI from the LSMA of SSM/I images was actually correct. Though, the LSMA calculation of melt index was satisfactory given the large bias of the Boolean calculation products. Figure 6 shows the maps of the original SSM/I *MI* (figure 6a), PMESDR *MI* (figure 6b), and the *MI* by unmixing calculation (figure 6c) for each land pixel. Compared with the high resolution PMESDR MI map (figure 6b), the overestimation of the SSM/I MI (figure 6a) mainly occurred on the Larsen Ice Shelf and the coast of Wilkins. The unmixing result (figure 6c) had overestimation on the Larsen Ice Shelf but underestimation on the Wilkins Ice Shelf. The overall pattern of the LSMA *MI* map matches the PMESDR *MI* map better, indicating a better accuracy of the estimated melt index from the unmixing method.

4.2. Impact of pixel size and endmembers purity on least squares mixture analysis

The LSMA model assumes the wet and dry pixels (figure 4b) picked from the study area are pure endmembers. However, with such a large pixel size of the 25-km SSM/I images, it would be difficult to find fully melted pixels. Therefore, we have to acknowledge that the endmembers of wet pixels could only be approximations and uncertainty could be brought to the LSMA model by the impurity of endmembers. Strictly, we may not be able to find real pure endmembers to implement the unmixing method at such a scale as satellite radiometer mapping. It is interesting to test, however, if some relaxation on the pure endmember selection criterion is acceptable and if the LSMA model can be improved by using the endmembers derived from the high resolution product rather than from the same SSM/I scene.

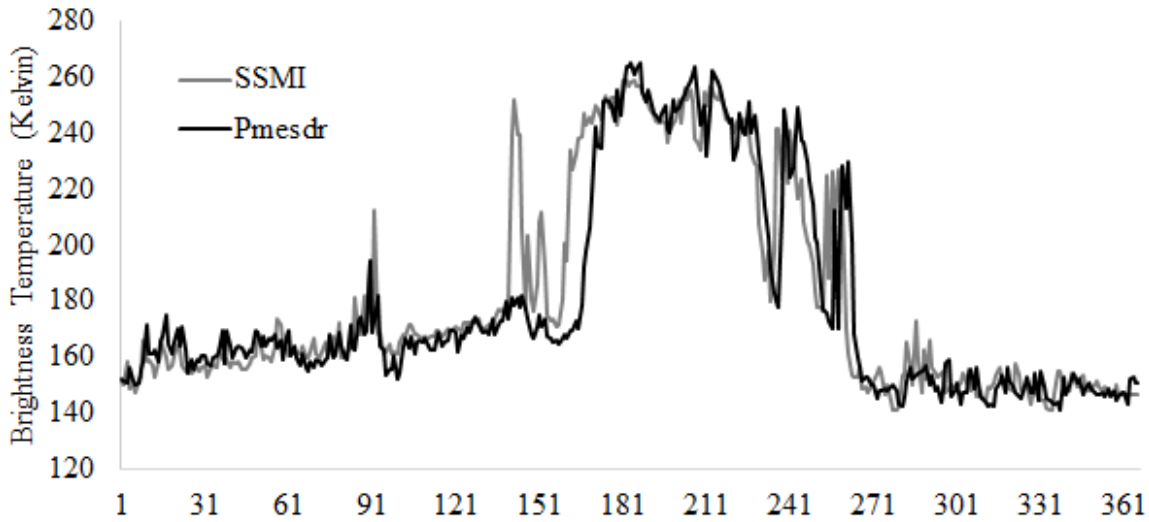

Figure 7: The comparison between the PMESDR pixel and the SSM/I pixel as endmembers.

Theoretically, the high resolution images should contain more pure pixels for the unmixing algorithm to use. To test how much the impurity of endmembers had impacted the unmixing results, we chose endmembers from the high resolution PMESDR images to implement the LSMA unmixing calculation. The PMESDR pixels were picked up from the center location of the SSM/I endmember pixels. As shown in figure 7, the PMESDR endmember has slightly higher brightness temperature values during the melting time. Then, the unmixing of the SSM/I

image was performed using the endmembers that were supposed to be more "pure" because the resolution of the PMESDR pixels was better. However, the unmixing results showed the RMSE of unmixing the SSM/I images using the PMESDR endmembers was 0.0088 (10^6 day·km^2), which was very close to but 6.02% higher than that using the SSM/I endmembers. Therefore, although the endmember impurity could cause uncertainty for unmixing, the endmembers obtained from the high resolution image did not improve the LSMA model. On the other hand, the high similarity between the unmixing results from SSM/I endmembers and the PMESDR endmembers indicates that the pixel resolution and impurity of endmembers did not bring much uncertainty to the LSMA model.

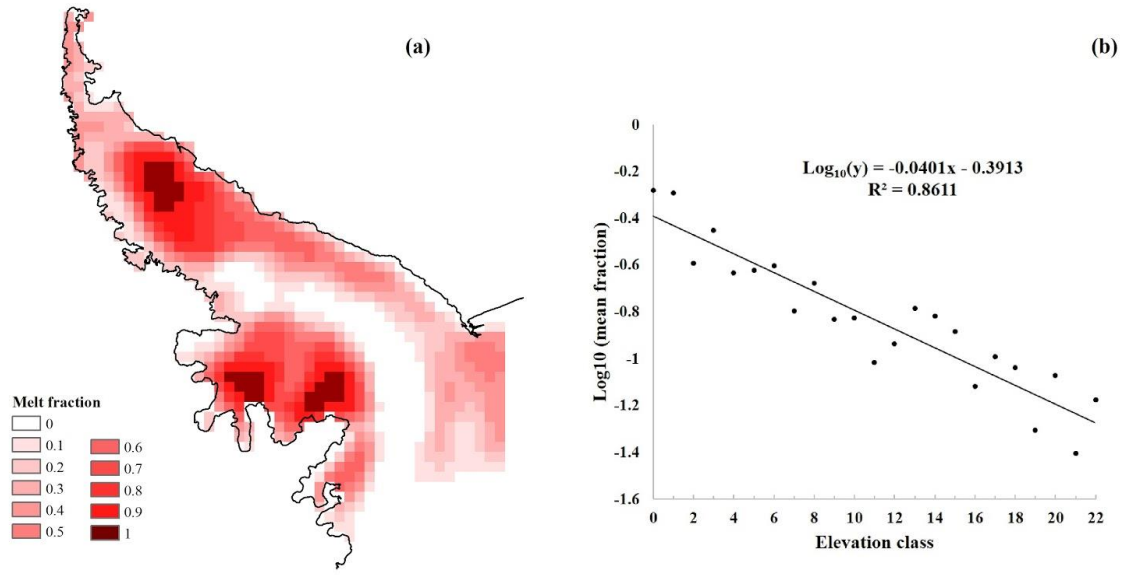

Figure 8: (a) The melt fraction map calculated from LSMA and (b) the scatterplot of between the melt fraction and mean elevation of the pixel.

4.3. Relationship with elevation

The spatial pattern of the melt fraction map in figure 8(a) shows a high resemblance with the topographic maps published for the Antarctic Peninsula. Therefore, we suspect the elevation may play an important role in the partial melting problem. We obtained a 1-km elevation model of Antarctica (Bamber et al., 2009) to analyze its correlation with the melt fraction map. In the scatterplot (figure 8b), each elevation class is defined by a 100-m interval from the lowest to the highest and named by the integer number rounded up from the 100th of their elevation values. In each elevation class, the mean melt fraction was calculated to make the scatterplot with the elevation class. Because of the non-linearity of the original scatterplot, a logarithm was taken on the mean melt fraction values. The melt fraction is almost 100% on the ice shelves near the coast and goes down sharply with the increasing elevation towards the mountains. The scatterplot shows a clear inverse log-linear trend ($p < 0.0001$) between the elevation class and the mean melt fraction. It suggests that, in the study area, the partial melting problem on the ice sheets is mainly caused by the elevation change. The logarithm relationship between elevation and melt fraction

indicates that the elevation has little impact on melt fraction over low-lying and flat ice shelves and, when the elevation is getting higher (e.g., 1000 m), it becomes a dominant variable to control partial melt fractions.

4.4. Unmixing the high resolution PMESDR images

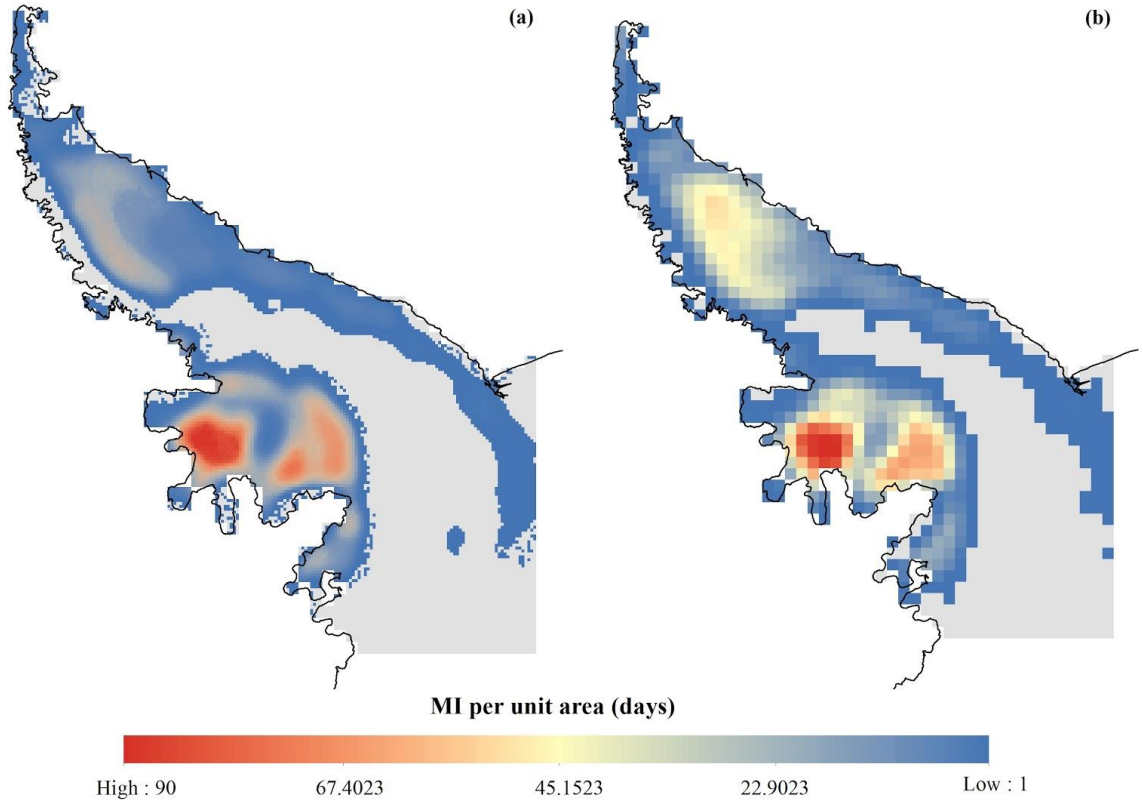

Figure 9: Subpixel melt index map from (a) PMESDR images and (b) original SSM/I images.

From the above discussions, we have proved the ability of LSMA to correct the bias introduced by the Boolean calculation of melt index. It is interesting to test how much difference is in the melt index derived from high resolution PMESDR images if the Boolean calculation was replaced by the LSMA model. The purpose of the test is to validate the application of LSMA to higher resolution image products. Therefore, we applied the same approach to the high resolution PMESDR images and compared the unmixed *MI* with that from the SSM/I images.

Figure 9a shows the melt index map from the LSMA calculation of PMESDR images using the spatially constrained endmembers. Compared to the unmixed melt index map from the original SSM/I images (figure 9b), the resolution and spatial details look much better. The melt index from the least squares mixture analysis for the whole study area was 4.417 (10^6 day·km^2), which is about 41.6% lower than the Boolean calculation *MI* from PMESDR. This difference is consistent with the comparison between the Boolean *MI* and unmixed *MI* from SSM/I images,

where the unmixed product was 43% lower. The overestimation bias of the Boolean calculation was therefore corrected by the LSMA method. We used the high resolution product of PMESDR images as a reference and confirmed such treatment improved the accuracy of the melt index estimation. Although owing to the unavailability of a higher resolution product than PMESDR data to verify its LSMA result, we can reasonably infer that the unmixed PMESDR melt index is the best map product for surface melt.

5. Conclusions

The large pixel size of passive microwave images has caused large uncertainty for monitoring surface melt over Antarctic Ice Margins. The melt maps need to be updated using high resolution data to reduce uncertainty. This paper proposes a least squares mixture analysis (LSMA) of the brightness temperature time series to calculate the subpixel melt index that is comparable with the high resolution products. We found that the map of Boolean surface melt derived from the SSM/I images could overestimate surface melt by 50% in Larsen and Wilkins Ice Shelves. With the treatment of LSMA, the overestimation of surface melt was offset and the uncertainty was also reduced.

The second finding from our analysis was that the unmixing method would reduce the *MI* estimate by a certain amount (e.g., 40-45% in our study area) regardless of the resolution of the image used. As the partial melting problem has caused overestimation of *MI*, the reduction of *MI* from the unmixing analysis was correct and necessary. Therefore, we recommend such an unmixing approach to be always applied to surface melt calculation from satellite radiometer data.

The third finding is that the melt fraction is inversely related to the elevation at a log-linear form. The log-linear regression equation between melt fraction and elevation suggests that the partial melting phenomenon in our study area could be largely controlled by topography on the high-elevation ice sheets. Therefore, partial melting of the passive microwave image pixels could be a severe problem for melt occurred near the Antarctic ice shelf grounding lines.

To illustrate and verify the time series unmixing method, we focused on the study area of the Antarctic Peninsula. With the evidence collected from this area, we will be able to generalize the application of the spatially constrained least squares mixture analysis to other major ice shelves of Antarctica and refine the trend analysis of Antarctic surface melt with higher confidence and less uncertainty.

Acknowledgments, Samples, and Data

This work was supported by the 2019 Manship Summer Research Fellowship of the College of Humanities and Social Sciences at Louisiana State University. The authors claim no real or perceived financial conflicts of interests. All datasets used in this research were obtained from the National Snow and Ice Data Center (NSIDC).

References

Abdalati, W., & Steffen, K. (1995). Passive microwave-derived snow melt regions on the Greenland Ice Sheet. *Geophysical Research Letters*, *22*(7), 787–790.

Abdalati, W., & Steffen, K. (1997). Snowmelt on the Greenland Ice Sheet as Derived from Passive Microwave Satellite Data. *Journal of Climate*, *10*(2), 165–175.

Abdalati, W., & Steffen, K. (2001). Greenland ice sheet melt extent: 1979--1999. *Journal of Geophysical Research, D: Atmospheres*, *106*(D24), 33983–33988.

Armstrong, R., Knowles, K., Brodzik, M. J., & Hardman, M. A. (1994). DMSP SSM/I-SSMIS Pathfinder Daily EASE-Grid Brightness Temperatures, Version 2, Southern Hemisphere [Data set]. https://doi.org/10.5067/3EX2U1DV3434

Bamber, J. L., Gomez-Dans, J. L., & Griggs, J. A. (2009). A new 1 km digital elevation model of the Antarctic derived from combined satellite radar and laser data – Part 1: Data and methods. *The Cryosphere*. https://doi.org/10.5194/tc-3-101-2009

Bhattacharya, I., Jezek, K. C., Wang, L., & Liu, H. (2009). Surface melt area variability of the Greenland ice sheet: 1979–2008. *Geophysical Research Letters*, *36*(20), 165.

Brodzik, M. J., & Long, D. G. (2015). Calibrated Passive Microwave Daily EASE-Grid 2.0 Brightness Temperature ESDR (CETB): Algorithm Theoretical Basis Document. *MEaSUREs Project White Paper*.

Brodzik, M. J., Long, D. G., Hardman, M. A., Paget, A., & Armstrong, R. (2018). MEaSUREs Calibrated Enhanced-Resolution Passive Microwave Daily EASE-Grid 2.0 Brightness Temperature ESDR, Version 1 [Data set]. https://doi.org/10.5067/MEASURES/CRYOSPHERE/NSIDC-0630.001

van den Broeke, M. (2005). Strong surface melting preceded collapse of Antarctic Peninsula ice shelf. *Geophysical Research Letters*, *32*(12). Retrieved from https://agupubs.onlinelibrary.wiley.com/doi/abs/10.1029/2005GL023247

Chein-I Chang, Hsuan Ren, Chein-Chi Chang, D'Amico, F., & Jensen, J. O. (2004). Estimation of subpixel target size for remotely sensed imagery. *IEEE Transactions on Geoscience and Remote Sensing: A Publication of the IEEE Geoscience and Remote Sensing Society*, *42*(6), 1309–1320.

De Freitas, M. W. D., Mendes Júnior, C. W., Arigony-Neto, J., Costi, J., & Simões, J. C. (2018). A multiscale subpixel mixture analysis applied for melt detection using passive microwave and radar scatterometer image time series of the Antarctic Peninsula (1999–2009). *Annals of Glaciology*, *59*(76pt1), 16–28.

Doake, C. S. M., & Vaughan, D. G. (1991). Rapid disintegration of the Wordie Ice Shelf in response to atmospheric warming. *Nature*, *350*(6316), 328–330.

Fahnestock, M. A., Abdalati, W., & Shuman, C. A. (2002). Long melt seasons on ice shelves of the Antarctic Peninsula: an analysis using satellite-based microwave emission measurements. *Annals of Glaciology*, *34*, 127–133.

Gilbert, R., & Domack, E. W. (2003). Sedimentary record of disintegrating ice shelves in a warming climate, Antarctic Peninsula. *Geochemistry, Geophysics, Geosystems*, *4*(4), 206.

Golledge, N. R., Keller, E. D., Gomez, N., Naughten, K. A., Bernales, J., Trusel, L. D., & Edwards, T. L. (2019). Global environmental consequences of twenty-first-century ice-sheet melt. *Nature*, *566*(7742), 65–72.

Holland, P. (2010). Warm bath for an ice sheet. *Nature Geoscience*, *3*(3), 147–148.

Liang, L., Li, X., & Zheng, F. (2019). Spatio-Temporal Analysis of Ice Sheet Snowmelt in Antarctica and Greenland Using Microwave Radiometer Data. *Remote Sensing*, *11*(16), 1838.

Liu, H., Wang, L., & Jezek, K. C. (2005). Wavelet-transform based edge detection approach to derivation of snowmelt onset, end and duration from satellite passive microwave measurements. *International Journal of Remote Sensing*, *26*(21), 4639–4660.

Liu, H., Wang, L., & Jezek, K. C. (2006). Spatiotemporal variations of snowmelt in Antarctica derived from satellite scanning multichannel microwave radiometer and Special Sensor Microwave Imager data (1978–2004). *Journal of Geophysical Research*, *111*(F1), 787.

Long, D. G., & Brodzik, M. J. (2016). Optimum Image Formation for Spaceborne Microwave Radiometer Products. *IEEE Transactions on Geoscience and Remote Sensing: A Publication of the IEEE Geoscience and Remote Sensing Society*, *54*(5), 2763–2779.

Long, D. G., & Daum, D. L. (1998). Spatial resolution enhancement of SSM/I data. *IEEE Transactions on Geoscience and Remote Sensing: A Publication of the IEEE Geoscience and Remote Sensing Society*, *36*(2), 407–417.

MacAYEAL, D. R., Scambos, T. A., Hulbe, C. L., & Fahnestock, M. A. (2003). Catastrophic ice-shelf break-up by an ice-shelf-fragment-capsize mechanism. *Journal of Glaciology*, *49*(164), 22–36.

Mote, T. L., & Anderson, M. R. (1995). Variations in snowpack melt on the Greenland ice sheet based on passive-microwave measurements. *Journal of Glaciology*, *41*(137), 51–60.

Mote, T. L., Anderson, M. R., Kuivinen, K. C., & Rowe, C. M. (1993). Passive microwave-derived spatial and temporal variations of summer melt on the Greenland ice sheet. *Annals of Glaciology*, *17*, 233–238.

NOAA. (2019, October 15). NOAA/NGDC - Earth Observation Group - Defense Meteorological Satellite Program, Boulder. Retrieved March 21, 2020, from https://ngdc.noaa.gov/eog/sensors/ssmi.html

Oza, S. R. (2015). Spatial–temporal patterns of surface melting observed over Antarctic ice shelves using scatterometer data. *Antarctic Science / Blackwell Scientific Publications*, *27*(4), 403–410.

Ridley, J. (1993). Surface melting on Antarctic Peninsula ice shelves detected by passive microwave sensors. *Geophysical Research Letters*, *20*(23), 2639–2642.

Scambos, T. A., Hulbe, C., Fahnestock, M., & Bohlander, J. (2000). The link between climate warming and break-up of ice shelves in the Antarctic Peninsula. *Journal of Glaciology*, *46*(154), 516–530.

Steffen, K. (1995). Surface energy exchange at the equilibrium line on the Greenland ice sheet during onset of melt. *Annals of Glaciology*, *21*, 13–18.

Steig, E. J., Schneider, D. P., Rutherford, S. D., Mann, M. E., Comiso, J. C., & Shindell, D. T. (2009). Warming of the Antarctic ice-sheet surface since the 1957 International Geophysical Year. *Nature*, *457*(7228), 459–462.

Tedesco, M. (2009). Assessment and development of snowmelt retrieval algorithms over Antarctica from K-band spaceborne brightness temperature (1979–2008). *Remote Sensing of Environment*, *113*(5), 979–997.

Torinesi, O., Fily, M., & Genthon, C. (2003). Variability and Trends of the Summer Melt Period of Antarctic Ice Margins since 1980 from Microwave Sensors. *Journal of Climate*, *16*(7), 1047–1060.

Vaughan, D. G., & Doake, C. S. M. (1996). Recent atmospheric warming and retreat of ice shelves on the Antarctic Peninsula. *Nature*, *379*(6563), 328–331.

Wang, L., & Liu, H. (2017). Seasonal melt extent and duration [in "State of the Climate in 2016"]. *Bulletin of the American Meteorological Society*, *98*(8), S162–S163.

Zwally, H. J. (2002). Surface Melt-Induced Acceleration of Greenland Ice-Sheet Flow. *Science*. https://doi.org/10.1126/science.1072708

Zwally, H. J., & Fiegles, S. (1994). Extent and duration of Antarctic surface melting. *Journal of Glaciology*, *40*(136), 463–475.

Zwally, H. J., & Gloersen, P. (1977). Passive microwave images of the polar regions and research applications. *The Polar Record*, *18*(116), 431–450.